

High-voltage operation reveals surface reconstruction as primary contributor to impedance growth over CEI evolution in Ni-Rich layered oxides

Steffen Schröder^{a,b,†}, Kilian Vettori^{b,c,†,*}, Lara Ahrens^{d,e}, Torsten Brezesinski^f, Aleksandr Kondrakov^{f,g}, Joachim Mayer^{d,e}, Jürgen Janek^{b,c,f,*}, Anja Henss^{a,b,*}

^a Institute of Experimental Physics I, Justus Liebig-University Giessen, Heinrich-Buff-Ring 16, 35392 Giessen, Germany

^b Center for Materials Research (ZfM), Justus Liebig-University Giessen, Heinrich-Buff-Ring 16, 35392 Giessen, Germany

^c Institute of Physical Chemistry, Justus Liebig-University Giessen, Heinrich-Buff-Ring 17, 35392 Giessen, Germany

^d Central Facility for Electron Microscopy (GFE), RWTH Aachen University, Ahornstr. 55, 52074 Aachen, Germany

^e Ernst Ruska-Centre for Microscopy and Spectroscopy with Electrons (ER C), Forschungszentrum Jülich GmbH, Wilhelm-Johnen-Straße, 52428 Jülich, Germany

^f Battery and Electrochemistry Laboratory (BELLA), Institute of Nanotechnology, Karlsruhe Institute of Technology (KIT), Kaiserstr. 12, 76131 Karlsruhe, Germany

^g BASF SE, Carl-Bosch-Str. 38, Ludwigshafen 67056, Germany

ARTICLE INFO

Keywords:

Lithium-ion batteries (LIB)

Nickel-rich NCM

High-voltage

Cathode electrolyte interphase (CEI)

Charge transfer resistance

ABSTRACT

Enhancing the energy density of lithium-ion batteries by increasing the nickel content in layered oxides as cathode materials is hindered by accelerated degradation at high potentials. Here, we resolve the degradation mechanism of single-crystalline $\text{LiNi}_{0.83}\text{Co}_{0.11}\text{Mn}_{0.06}\text{O}_2$ (NCM) by comparing different aging protocols, varying upper cutoff voltage, time exposed to high potential (4.5 V *versus* Li^+/Li) and number of cycles. The impedance growth due to these stressors is quantified by electrochemical analysis, including potentiostatic electrochemical impedance spectroscopy (PEIS). The structural and chemical degradation is investigated *post mortem* via transmission electron microscopy (TEM), X-ray photoelectron spectroscopy (XPS), and secondary ion mass spectrometry (SIMS). The analysis reveals that the organic components of the CEI are oxidized and removed during extended holds at 4.5 V. However, this CEI thinning occurs alongside an increase in charge transfer resistance R_{CT} . Furthermore, cells undergoing cycling *versus* hold protocols exhibited similar CEI compositions despite different R_{CT} . Therefore, we conclude that the CEI plays a minor role in the observed impedance increase. In contrast, the formation of a rock-salt-type SRL correlates with kinetic limitations and capacity fade. These findings provide a basis for distinguishing the effects of CEI evolution from surface reconstruction during long-term, high-voltage operation.

1. Introduction

Lithium-ion batteries (LIBs) first reached the broad consumer market in small electronic handheld devices and are now central to the transition from combustion engines to electric vehicles (EVs) and will play a major role in the electrification of homes and industry soon. The limited space for the battery in most EVs and future robots creates a persistent demand to increase the energy density of LIBs. For layered oxide cathodes, this can be achieved on the material level by increasing the nickel content, which results in more available capacity in the typical voltage range of 3.0 V – 4.3 V *versus* Li^+/Li .

This strategy has driven the evolution of cathode active materials (CAMs) from the initial LiCoO_2 (LCO) to mixed layered oxides like $\text{LiNi}_a\text{Co}_b\text{Mn}_c\text{O}_2$ (NCM), where the nickel content was increased above 80% over the years in so-called high-Ni NCMs. Yet, the higher nickel content in these materials comes at the cost of an increased rate of degradation during battery operation [1–5].

In real world applications, the battery is exposed to different currents, voltages, discharge depths, and temperatures during operation. All these factors have a different effect on degradation of the battery. Generally speaking, higher C-rate, higher cut-off potential (U_{UC}) or higher state of charge (SoC), and higher temperature lead to a faster

* Corresponding authors at: Center for Materials Research (ZfM), Justus Liebig-University Giessen, Heinrich-Buff-Ring 16, 35392 Giessen, Germany.

E-mail addresses: kilian.vettori@uni-giessen.de (K. Vettori), juergen.janek@phys.chemie.uni-giessen.de (J. Janek), anja.henss@uni-giessen.de (A. Henss).

† Both authors contributed equally to this work.

capacity fading in the battery cell [2,6–13]. Sometimes less degradation is observed for higher C-rates [9,10], which can be explained by the shorter time at high potentials t_{hold} and SoC. The most damaging factor of all those is a high cut-off potential, because multiple degradation mechanisms are triggered simultaneously. A high potential not only drives the formation of resistive phases (the cathode electrolyte interphase (CEI) and a surface reconstruction layer (SRL) consisting of rocksalt-type phase) but also promotes transition metal (TM) dissolution into the electrolyte. The dissolved TM ions damage the solid electrolyte interphase (SEI) of the anode, leading to a rapid loss of cyclable lithium [14,15]. This shows that multiple degradation mechanisms can be the cause for capacity decay. Which degradation effect plays the most critical role cannot be identified only on the basis of the capacity retention and potential-charge curve of the full cell. Therefore, detailed complementary electrochemical and advanced analytical techniques are required, through which four main degradation mechanisms of layered oxides have been identified in the literature [16,17]. These mechanisms are the focus of the present study.

Typical degradation processes in high-Ni NCM include particle cracking, transition metal dissolution, structural degradation (e.g., SRL or defect formation), and the formation of a CEI. These phenomena occur at different stages of battery operation and contribute differently to performance loss, which manifests as capacity fade and/or an increase in cathodic impedance. A key challenge is to understand which of these processes is primarily responsible for the rise in charge-transfer impedance (R_{CT}), though evidence suggests that the thickening of the CEI and the formation of the SRL are major contributors [18–23].

The overall degradation process results from a complex interplay. It is well understood that these phenomena are driven by distinct operational stressors, including state of charge, temperature, and cycling rate. In the following, we briefly summarize the literature to identify those most relevant for NCM degradation. **Particle cracking** is a mechanical failure mainly caused by the internal stress from anisotropic volume changes during cycling, especially at high potentials above 4.1 V, where the H2-H3 transition is observed in LiNiO_2 (LNO). In conventional polycrystalline materials, this stress leads to intergranular cracks between the primary particles, often within the first few cycles, which can also lead to the loss of active material due to contact loss [24–26]. High C-rates intensify this cracking by creating larger lithium-ion concentration gradients that increase the local mechanical stress [13,18]. The main consequence of these cracks is the exposure of fresh, unprotected cathode surface to the electrolyte, which in turn leads to more side reactions. On these newly exposed surfaces, and on the original particle surface, additional degradation mechanisms are triggered. **Structural degradation** leads to an irreversible phase transformation from the layered structure to an inactive rocksalt-type phase. This is initiated by cation mixing, where Ni^{2+} ions migrate into lithium sites, a process that is most severe at high potentials (above 4.3 V *versus* Li^+/Li) and elevated temperatures [1,22,27–30]. This structural transition to a rocksalt-type phase (from TMO_2 to TMO) also involves the evolution of lattice oxygen, possibly in form of singlet oxygen [31–33]. High C-rates have a minor effect, but can promote this degradation by creating localized currents at the surface, exposing it to more damaging conditions [11]. The inherent instability at high potentials, combined with the newly exposed surfaces from cracking, also increases the **dissolution of transition metals**. This process is driven by chemical attack from acidic species like hydrofluoric acid, which forms from electrolyte decomposition, and is significantly accelerated at higher temperatures and slightly increased at high states of charge [19,34]. Finally, the highly oxidizing nature of the transition metal oxide surface and the oxygen release of the irreversible phase transformation lead the continuous decomposition of the electrolyte to form the **cathode electrolyte interphase (CEI)**. It is often claimed, that this CEI layer is also a major contributor to the overall cell impedance [2,21,35]. The evolution and composition of the CEI during battery operation is mainly dependent on the cut-off voltage during operation and also on temperature [36–41].

The degradation pathway of a given layered oxide is governed by a complex interplay of operational parameters such as C-rate, potential, number of cycles, and temperature. Among these, high potential is identified as the most critical factor driving oxygen loss, structural degradation toward a rocksalt-type phase and promoting CEI growth. In contrast, cycling primarily induces chemo-mechanical fatigue, leading to particle cracking through the repetitive stress associated with the H2-H3 transition.

This study builds upon our previous work, in which it was investigated the time dependent degradation of Ni-rich NCM under constant high potential conditions [42]. Here, we try to clarify the respective roles of the CEI and SRL in driving the interfacial degradation of high-nickel cathodes. A key objective is to investigate whether potentiostatic holds at high potentials or dynamic cycling induces more severe degradation. To this end, we compare cathodes subjected to different cycling routines that we understand as in accelerated-aging tests [40]. We varied parameters such as upper potential limit (U_{UC}), hold time at 4.5 V (t_{hold}), and number of cycles to investigate how these distinct stressors influence CEI and SRL evolution. The resulting material-level changes are correlated with the observed cathodic impedance (mainly R_{CT}) and capacity fade. In order to achieve this, we analyze a commercial high-Ni single-crystalline CAM, i.e., NCM831106, using different techniques. We monitor electrochemical behavior with potentiostatic electrochemical impedance spectroscopy (PEIS). Subsequently, we use *post mortem* X-ray photoelectron spectroscopy (XPS) and secondary ion mass spectrometry (SIMS) to track alterations of the CEI, while transmission electron microscopy (TEM) is used to examine the local crystal structure at the particle surface. In contrast to models focusing primarily on the CEI, our study highlights the impact of SRL as a significant factor in the charge transfer resistance R_{CT} growth of Ni-rich cathodes, under these specific high-voltage conditions. We further reveal that this degradation is triggered more by dynamic cycling than by extended potential holds.

2. Results and discussion

2.1. Electrochemistry

To unravel the degradation of high-Ni NCM induced by high potential holds and cycling itself, different cycling protocols with various upper cut-off potentials U_{UC} , hold times t_{hold} at $U_{\text{UC}} = 4.5$ V, and number of cycles were tested both in 2-electrode (coin cell) and 3-electrode (pouch cell with lithiated gold wire reference) configurations. All potentials are given *versus* the Li^+/Li potential. $U_{\text{UC}} = 4.5$ V was chosen in accordance with our previous publication. This is intentionally slightly above the onset potential for oxygen release at $\sim 80\%$ SoC for high-Ni NCMs (4.4 V for NCM811) [32,33,43], which was shown by online electrochemical mass spectrometry (OEMS) [42]. In our previous study, the most prominent form of cathode degradation due to high potential holds was of kinetic nature, characterized by linear capacity fading and nonlinearly increasing R_{CT} . This was especially prominent at high and low potentials, where kinetics is already slow. This was mainly attributed to inhomogeneous coverage of the particle surface regions with a rocksalt-type phase and thus a constriction of Li-ion pathways.

Here, the effect of additional cycling on these phenomena is investigated. Table 1 (in experimental section) summarizes the different electrochemical protocols and respective cathode samples: “4.3 V cyc”, “4.5 V cyc”, “4.5 V hold”, “4.5 V cyc+hold”, where “4.5 V hold” data is taken from [42]. We chose this labelling to show the focus of the cycling protocol, while cycling is done in constant current (CC) and holding in constant voltage (CV) mode. Fig. 1a shows the respective discharge capacity retention data. After initial formation, all protocols lead to linear capacity fading. Increasing U_{UC} from 4.3 V to 4.5 V increases its slope as is well visible when comparing the blue and light red curve. The fading is similar compared to the 0.1C data of the “4.5 V hold” cell in yellow where each cycle has a 2 d hold at 4.5 V. The strongest capacity

Table 1

Cathode samples used for *post mortem* analysis and respective electrochemical protocols. For more details (also 3-electrode cells) refer to Table S1 (Reference [42] is cited in Table body part).

sample	U_{UC} / V	t_{hold} / d	# cycles	description
pristine	-	-	-	Punched and pressed cathode
OCV	-	-	-	Cathode from cell which was kept at OCV for 37 d
4.3 V cyc	4.3	-	103	Formation, then 100 cycles (0.5C charge to U_{UC} , 1C discharge to 3 V), final 0.1C cycle
4.5 V hold	4.5	16	11	Formation, then 9 PEIS check-up cycles (0.1C charge with hold and PEIS at 3.0, 3.7, 4.0, 4.3 and 4.5 V, hold at U_{UC} for 48 h, 0.1C discharge to 3 V) (data for this procedure is taken from [42]).
4.5 V cyc	4.5	1.8	103	Formation, then 100 cycles (0.5C charge to U_{UC} , 1C discharge to 3 V), final 0.1C cycle
4.5 V cyc+hold	4.5	16	103	Formation, then 100 cycles (0.5C charge to U_{UC} , hold at U_{UC} for 230 min, 1C discharge to 3 V), final 0.1C cycle

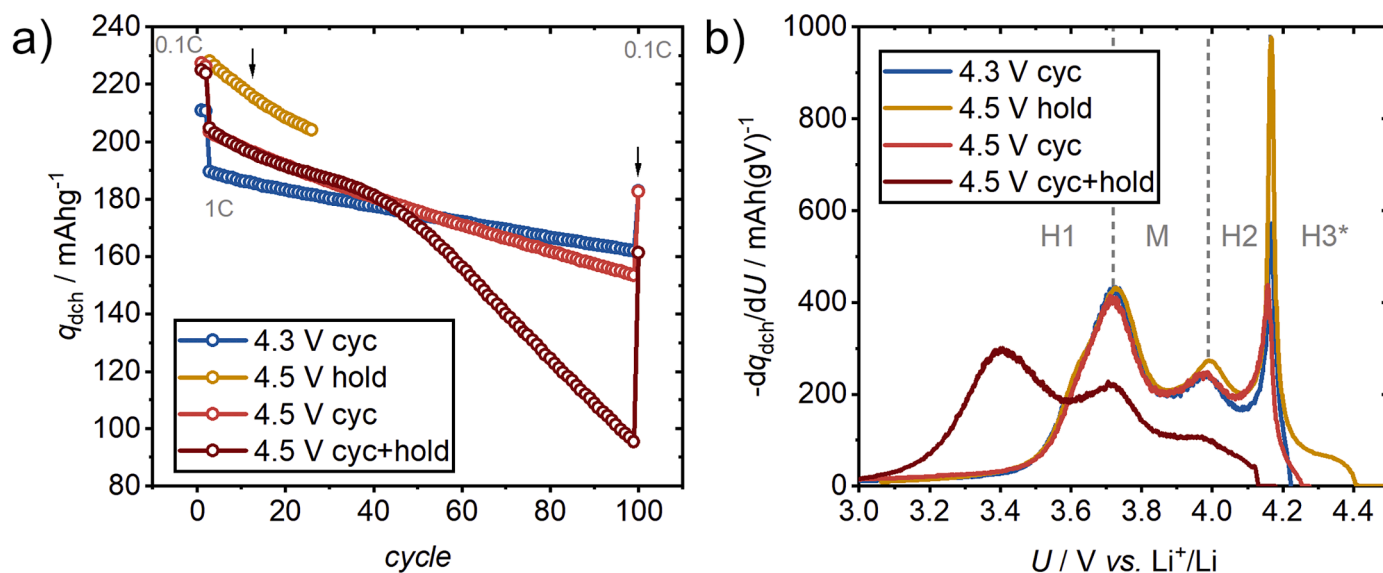


Fig. 1. Electrochemical behavior of scNCM831106 subjected to various cycling protocols. a) Specific discharge capacity over the course of cycling. For the protocols, the time at 4.5 V differs according to Table 1. b) dq/dU calculated for 0.1C discharges from a), indicated by black arrows.

loss is visible for the dark red curve (“4.5 V cyc+hold”). Here, a strong capacity fade after ≈ 40 cycles is observed, meaning the initial fading (1C discharge) of $0.57 \text{ mAhg}^{-1}/\text{cycle}$ is almost tripled to $1.57 \text{ mAhg}^{-1}/\text{cycle}$. The onset of this stronger decay corresponds with the point where kinetic limitations (also in the form of overpotentials) shift the extracted capacity below the lower cutoff-potential of 3.0 V for 1C cycles. More details are given in the Supporting Information (SI) section S2.1. The final 0.1C checkup cycles in Fig. 1a show that major parts of the capacity can be recovered for all protocols. Compared to the 2nd formation cycle, “4.3 V cyc”, “4.5 V cyc” and “4.5 V cyc+hold” show 86.8, 80.7 and 72.1% retention, respectively. From each of the samples, dq/dU of the discharge is calculated at the cycles indicated with black arrows. The cycle of the “4.5 V hold” cell was chosen, so that yellow and

dark red curves have similar $t_{hold} \approx 16 \text{ d}$.

Fig. 1b presents the dq/dU plots, which serve as diagnostic tool for the analysis of CAM degradation. The potential curves (2nd and final 0.1C cycle) from which dq/dU was calculated are also given in SI section S2.1. Fig. 1b shows only minor differences between “4.3 V cyc”, “4.5 V cyc” and “4.5 V hold”, which are caused by different U_{UC} and t_{hold} . The hold cell (“4.5 V hold”) still shows a small shoulder to the left of the M→H1 transition peak corresponding to the kinetic hindrance of lithium diffusion at high degrees of lithiation/low potentials. The strongest degradation is visible in the cell that experienced multiple cycles and holds, i.e. the dark red curve (“4.5 V cyc+hold”). A strong potential drop at the beginning of discharge of $\approx 350 \text{ mV}$ compared to $\approx 100 \text{ mV}$ (“4.5 V hold”) is observed, so that the remnant of the H3→H2 transition peak

(typically ≈ 4.2 V) is not visible anymore. The H₂→M (≈ 4.0 V) and M→H₁ (≈ 3.7 V) transition peaks are broadened and diminished in height but interestingly not shifted by the potential drop. This indicates that the initial potential drop is not due to ohmic resistances but rather that delithiation to high SoCs is kinetically hindered. A new peak at ≈ 3.4 V appears in the strongly degraded “4.5 V cyc+hold” sample. The attribution of peaks is supported by the gradual evolution of dq/dU plots in 3-electrode cells shown in SI section S2.2. We believe the new peak corresponds to “delayed” capacity due to strong kinetic hindrance as the coulometric titration curve of the aged cathode has a similar shape to a cathode after formation (SI section S2.3 and S2.4). The stronger fading, the delayed capacity and the observed loss of active material could be interpreted as indicators of a covering, resistive layer on the CAM surface. For an estimation of the maximum loss of CAM, we compared titration curves of 3-electrode cells after formation and after the “4.5 V cyc+hold” procedure, resulting in an upper estimation value of $\approx 10\%$ (SI section S2.3).

To summarize, the data in Fig. 1 reveal strong degradation mainly due to slow kinetics but also due to loss of active material. The kinetic hindrance was quantified via PEIS measurements in 3-electrode cells, allowing access to the charge transfer resistance R_{CT} of the cathode. For that, similar cycling protocols (“4.5 V cyc”, “4.5 V hold”, “4.5 V cyc+hold”) were applied. Please note that the protocols varies slightly from the 2-electrode measurements as 0.1C checkup cycles were included to measure PEIS (Table S1). The increase of mass normalized R_{CT} at 4.0 V during the selected protocols is shown in Fig. 2 against the two main stressors, the number of cycles and the time t_{hold} at $U_{UC} = 4.5$ V. PEIS is also measured at 3 V, 3.7 V, 4.0 V, 4.3 V and 4.5 V, each after at least 2 h of hold time for stability. More detailed EIS data and info regarding normalization and evaluation are given in SI section S2.4.

All three types of samples show initial nonlinear growth in R_{CT} which becomes more linear at later cycles or longer t_{hold} . The origin of the strong capacity decay of the “4.5 V cyc+hold” sample becomes plausible in Fig. 2 where R_{CT} increases drastically during additional cycling. For more details refer to full cycling data of the cells in SI section S2.2.

After 25 cycles (vertical line in Fig. 2b), R_{CT} increases by factors of 4.5, 5.0, and 29.4 for “4.5 V cyc”, “4.5 V cyc+hold”, and “4.5 V hold”, respectively. These differences arise from varying t_{hold} at 4.5 V of 0.5,

3.7, and 44 days. After t_{hold} of ≈ 16 d (horizontal line in Fig. 2b), “4.5 V cyc” results in an increase by a factor of 6.6, while “4.5 V cyc+hold” shows a substantially larger 136-fold increase. A t_{hold} of ≈ 16 d corresponds to the final conditions of the 2-electrode measurements and the subsequent *post-mortem* analyses. It also appears as if the linear regime of R_{CT} growth occurs at shorter t_{hold} if more cycling occurs.

Overall, Fig. 2b indicates that, within the investigated parameter space, cycling is the dominant factor governing the evolution of R_{CT} . Here, it has to be noted that holding and cycling can have interacting effects. *E.g.*, if during holding more CAM transitions to a phase with slow Li diffusion (*e.g.*, H₃) and the subsequent discharge induces strong Li concentration gradients and thus stress within the crystal.

The electrochemical measurements clearly demonstrate that the combination of cycling and high potential holds (CV) results in severe degradation. This includes rapid yet linear capacity fading, substantial overpotentials, loss of active material and a steep increase in R_{CT} . To investigate the possible reasons for the elevated R_{CT} , *post mortem* analyses were conducted.

2.2. Chemical composition of cathode electrolyte interphase (CEI)

To investigate the chemical evolution of the cathode surface under chosen aging protocols, a combination of XPS, ToF-SIMS and Orbitrap-SIMS was employed. The sample preparation and sample labels are detailed in the experimental section and in Table 1.

Fig. 3 presents the C 1 s, O 1 s, and Li 1 s core-level spectra for the prepared cathodes. An offset is added to the spectra for better visibility. Evaluation of XP spectra is based on several publications about NCM degradation [36,38,39,41,44,45]. The F 1 s, P 2p, and Ni 2p detail spectra are given in the SI section S4.

The Li 1 s spectra (Fig. 3) provide insight into the inorganic CEI components. The Li-NCM lattice signal at $E_B \approx 54.5$ eV is visible for the pristine sample and slightly visible as a shoulder for the “OCV”, “4.5 V hold”, and “4.5 V cyc+hold” samples. This indicates that the CEI for the pristine sample is thinner. In the region from $E_B = 55 - 57$ eV, signals for surface lithium species are observed. The “OCV” sample shows a distinct peak at ≈ 56.0 eV, characteristic of LiF formation during storage. For all cycled samples, this peak shifts slightly to lower binding energies (≈ 55.5

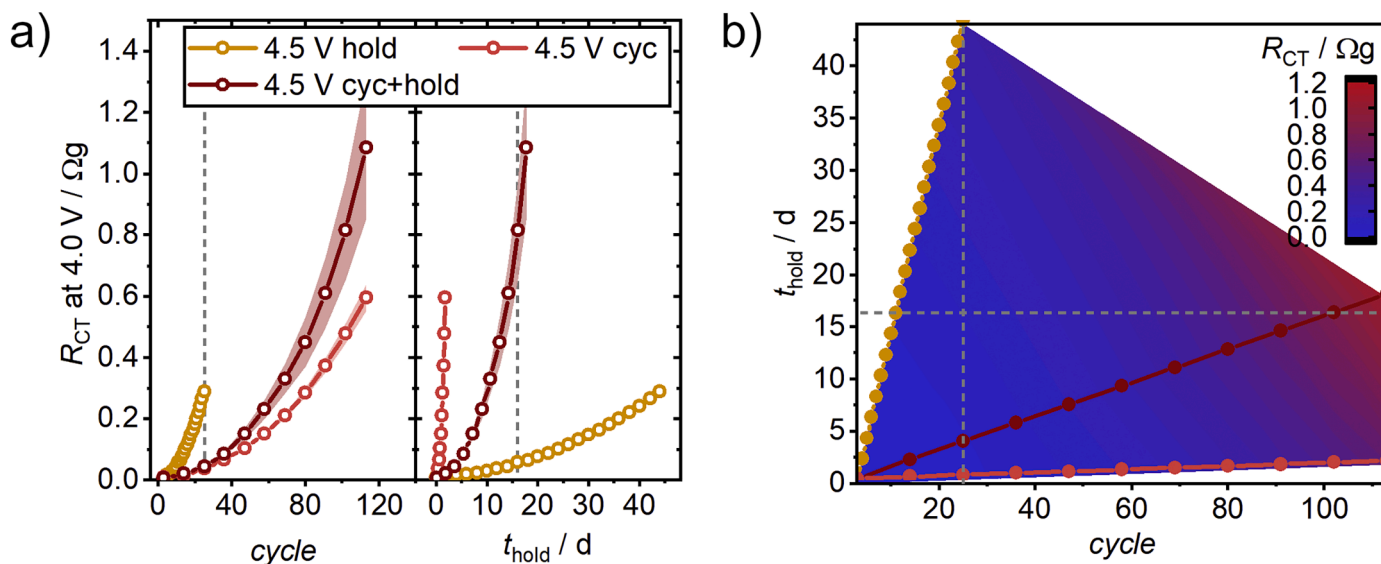


Fig. 2. Evolution of mass normalized charge transfer resistance R_{CT} at 4.0 V versus Li^+/Li of scNCM831106 subjected to various cycling protocols measured in 3-electrode cells. R_{CT} is obtained from fitting cathode impedance spectra with a simple $R-(R)(P)-(R_{CT})(P)$ model in Relaxis, where R denotes a resistor, P a constant-phase element, brackets a parallel and dashes a series connection. For fitting of impedance spectra and absolute R_{CT} values, see SI Section S2.4. a) R_{CT} against cycle and t_{hold} (time at $U_{UC} = 4.5$ V). Error bars correspond to standard deviation from the average of duplicate cells. b) Two-dimensional representation of the influence of cycle and t_{hold} on R_{CT} . Grey lines guide a comparison of R_{CT} if one of the parameters is kept constant, $t_{hold} \approx 16$ d corresponds to the 2-electrode protocols and the *post mortem* measurements.

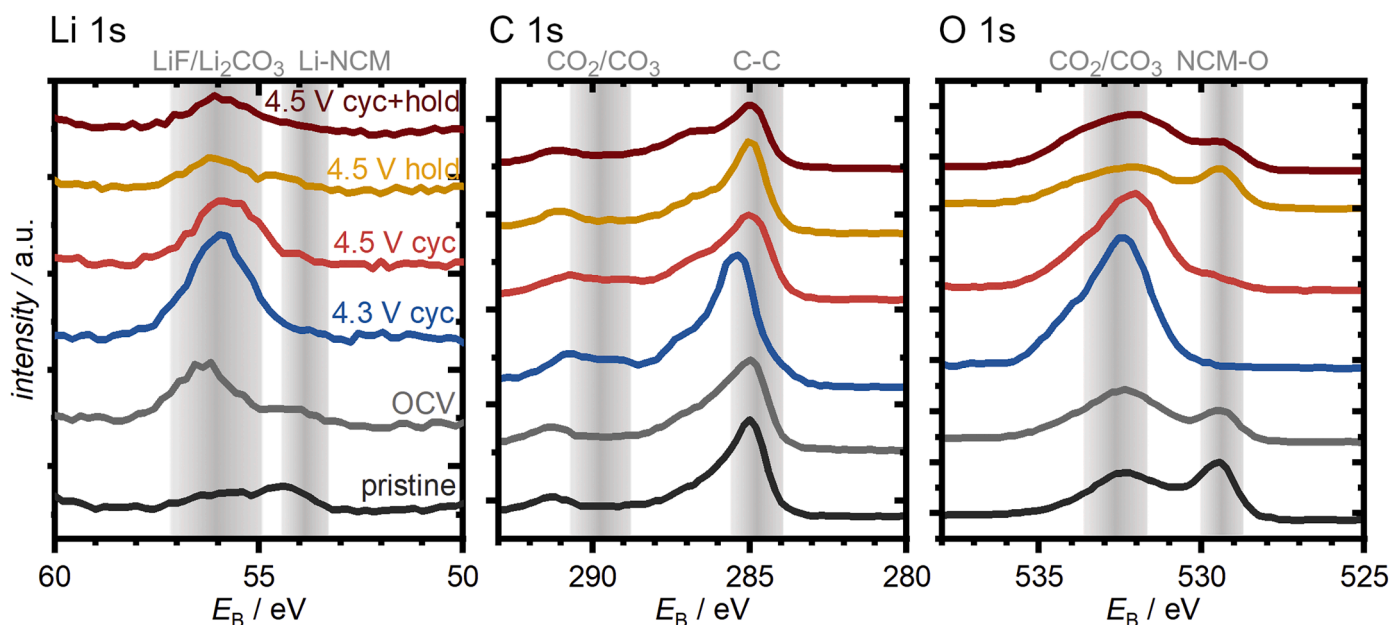


Fig. 3. XP detail spectra for Li 1 s, C 1 s and O 1 s. The spectra of various cathode samples are displayed: pristine (black), OCV for 37 d (grey), cycled with $U_{UC} = 4.3$ V (blue), $U_{UC} = 4.5$ V (light red), held at $U_{UC} = 4.5$ V for 16 days (yellow) and combined cycling and hold at $U_{UC} = 4.5$ V (dark red).

eV) and broadens, indicating the co-existence of Li_2CO_3 and LiF.

The C 1 s spectra (Fig. 3) reveal significant changes in the organic chemistry of the surface. All cathodes show the same type of signals in the range of $E_B = 285 - 293$ eV, only the ratio between those peaks is changing. The pristine and OCV samples are dominated by signals from adventitious carbon and conductive carbon additive (≈ 284.8 eV), with only a minor shoulder indicating some oxidized carbon species. Upon cycling to 4.3 V, a substantial increase in oxidized organic compounds is observed across the entire binding energy range. Specifically, a prominent shoulder develops at ≈ 286.5 eV, corresponding to C—O bonds, and the intensity at ≈ 290.0 eV, assigned to carbonate species (O—C=O), also increases. Interestingly, upon cycling to 4.5 V, the relative intensity of these oxidized organic signals, particularly the carbonate peak, decreases compared to the 4.3 V sample. This trend continues for the "4.5 V hold" and "4.5 V cyc+hold" samples, where the carbonate signal is further diminished, while a shoulder around 287 eV becomes more defined.

The O 1 s spectra (Fig. 3) show similar trends as observed in the C 1 s region. The intensity in the higher binding energy region (>532 eV), which contains contributions from organic C=O (≈ 532 eV) and C—O (≈ 533.5 eV) species, follows the same pattern: it is highest for the "4.3 V cyc" sample and decreases progressively for the samples aged at 4.5 V. Furthermore, the "4.5 V hold" and "4.5 V cyc+hold" samples exhibit a growing shoulder toward 534 eV, indicative of phosphorus-oxygen species (e.g., PO_xF_y), a known product of LiPF_6 degradation. Crucially, the signal at 529.5 eV, which is the signature of the transition metal-oxygen (TM-O) bonds in the NCM lattice, provides an indicator for the thickness of the surface layer. This signal vanishes for the "4.3 V cyc" sample, suggesting a CEI thickness that exceeds the XPS sampling depth (≈ 10 nm). In contrast, the TM-O signal reappears for the "4.5 V hold" sample and its intensity increases with longer t_{hold} at 4.5 V, indicating that the overall surface layer becomes thinner under prolonged exposure to high potentials.

To gain a more detailed chemical fingerprint of the cathode surfaces, ToF-SIMS surface spectra were collected. The single-ion counting capability of ToF-SIMS allows for the detection of individual molecular fragments, making it a highly sensitive method for monitoring surface modifications. The resulting ToF-SIMS surface spectra were analyzed using principal component analysis (PCA). The resulting score plot (Fig. 4) shows that the different cathode samples form distinct, well-

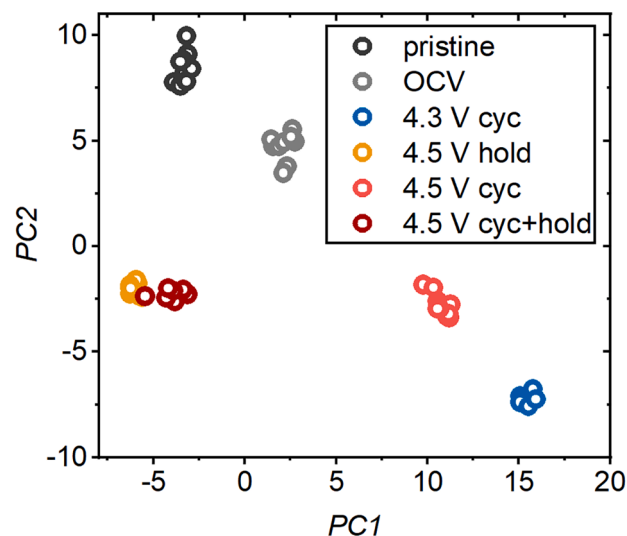


Fig. 4. Scatter plot of the principal components 1 and 2 from the PCA results of the ToF-SIMS surface spectra. Scores for principal components 1 and 2 of various cathode samples are displayed: pristine (black), OCV for 37 d (grey), cycled with $U_{UC} = 4.3$ V (blue), $U_{UC} = 4.5$ V (light red), held at $U_{UC} = 4.5$ V for 16 days (yellow), and combined cycling and hold at $U_{UC} = 4.5$ V (dark red).

separated clusters, confirming that each aging protocol produces a unique surface chemistry. The corresponding loading plots (see SI section S5.1) for Principal Component 1 (PC1) and 2 (PC2), were used to identify the characteristic secondary ion fragments responsible for this chemical separation.

Analysis of the loadings revealed that the pristine sample is defined by signals originating from the bulk cathode components, including the NCM (e.g., NiO^- , NiO_2^-), the PVdF binder (e.g., CF^-) and conductive carbon (e.g., C_8^-). After storage, the "OCV" sample changes significantly, driven by the appearance of hydrocarbon fragments originating from the electrolyte (e.g., C_2H_3^- , C_3H_3^- , C_4H_3^-), a strong increase in LiF (e.g., LiF_2^-) and slight increase in NiF_2^- (e.g., NiF_2^-), indicating the formation of an initial CEI. Additionally, the intensity of the NCM signal (e.g., NiO_2^-)

decreases.

The sample cycled to 4.3 V ("4.3 V cyc") evolves further, showing an increase in the intensity of oxidized organic fragments (e.g., C_2HO^- , $C_3H_5O^-$), lithiated organic species (e.g., CH_2Li^-) and other lithium-containing species (e.g., LiH_2^- , $LiOH^-$, LiO^-). On the other hand, the signal intensity of initially formed LiF decreases. This confirms the formation of a more developed, organic-rich CEI, as suggested by XPS.

Compared to the 4.3 V sample, the surface composition of the "4.5 V cyc" cathode shows a reduced contribution from the typical organic fragments. Instead, new signals emerge, including fluorinated metal species (NiF_2^-) and fragments from the fluorinated aluminum current collector (AlF_4^-). This trend is significantly amplified for the "4.5 V cyc+hold" and "4.5 V hold" samples, resulting in the separation of samples with hold steps into a distinct region of the score plot, which indicates their chemical similar CEI. For these cathodes, the scores are heavily influenced by highly oxidized species from conducting salt (e.g., PO_3^- , $LiPO_3F^-$).

Crucially, this change in chemical composition for the samples is accompanied by a relative increase in the intensity of the base NCM signals (NiO^- , NiO_2^-), a trend that strengthens with longer t_{hold} . This observation confirms the XPS results, indicating that the surface layer becomes thinner or less uniform under prolonged exposure to high potentials.

To obtain structural depth-resolved information of the chemical composition of the CEI, Orbitrap-SIMS was employed. This offers ultra-high mass resolution, enabling the accurate identification of higher-mass fragments. Furthermore, the mass analysis is largely independent of sample surface topography, effectively mitigating artifacts arising from surface roughness. The resulting depth profiles are presented in Fig. 5, with signal intensities normalized to the maximum intensity of the plotted fragments. The raw maximum counts as well as the depth profiles with raw counts are provided in SI section S5.2. The NiO_2^- fragment is used as a marker for the NCM active material, while NiF_2^- , $AlO_2H_2F_2^-$, and $C_2H_3O_2^-$ represent fluorinated CAM species, aluminum corrosion products, and organic electrolyte degradation products, respectively.

The profiles reveal a layered nanostructure of the CEI on all aged cathodes, generally with an outer organic-rich layer and an inner inorganic-rich layer. The "OCV" sample already shows a distinct, layered CEI containing significant amounts of both organic ($C_2H_3O_2^-$) and inorganic, namely fluorinated (NiF_2^-) species. Upon cycling to 4.3 V ("4.3 V cyc"), the CEI thickens, as evidenced by the delayed rise of the NiO_2^- NCM signal. The profiles also show that the distinct layers become more intertwined, suggesting a less defined, more mixed CEI nanostructure between the organic and inorganic regions. In contrast, the sample cycled to 4.5 V ("4.5 V cyc") exhibits a thinner CEI and a more sharply defined layered nanostructure. Alternatively, this thinning effect could be an artifact originating from a CEI that covers less of the CAM. In SI section S6, we explain why we assume that, in our case, this heterogeneity plays a minor role. There is a significant increase in aluminum-rich degradation products ($AlO_2H_2F_2^-$) and a slight increase in fluorinated CAM species (NiF_2^-). This trend is amplified for the "4.5 V hold" and "4.5 V cyc+hold" cathodes. Both samples show very similar depth profiles, characterized by a significant accumulation of degraded aluminum collector species and fluorinated CAM at the interface, while the signal from organic fragments decreased.

Considering the findings from XPS, ToF-SIMS, and Orbitrap-SIMS, we conclude that there is a significant difference in the chemical composition and thickness of the CEI on the differently treated cathodes, which is clearly due to the different operational stressors.

Our observations on the CEI evolution are consistent with the existing literature, and expand upon it. The general chemical components we identified, including LiF, organic species ($C_xH_yO_z$, C_xH_yOLi), salt degradation products ($Li_xPO_yF_z$), and fluorinated metal species from the NCM (NiF_2), are identical to those found in previous studies on high-Ni cathodes [36,38,39,41,44,45]. Likewise, the layered nanostructure of

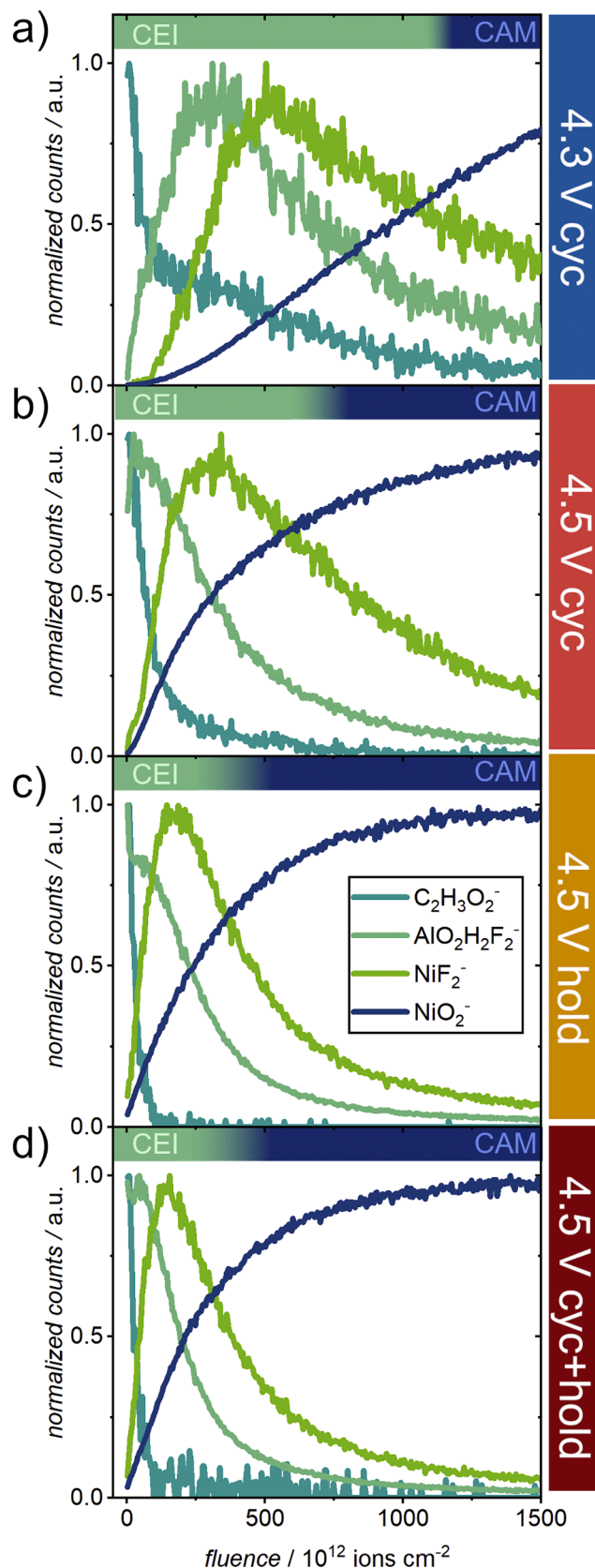


Fig. 5. Orbitrap-SIMS depth profiles of various cathodes are displayed: a) cycled with $U_{UC} = 4.3$ V (blue), b) $U_{UC} = 4.5$ V (light red), c) held at $U_{UC} = 4.5$ V for 16 days (yellow), and d) combined cycling and hold at $U_{UC} = 4.5$ V (dark red).

the CEI has been reported previously [37,38]. Regarding the overall CEI thickness, we find values in the range of 7–20 nm. This aligns with some reports [46], while other studies have described a much thicker CEI, sometimes in the range of 150–300 nm, making it more comparable in scale to the SEI at the anode [47]. The thinning of the CEI at higher potentials aligns with reports by Yu *et al.* and Luo *et al.*, who observed a similar reduction in thickness when increasing the cut-off potential from 4.1 V to 4.8 V [39,41]. The exact thinning mechanism and the fate of these oxidized CEI species remain a topic of discussion, as we explore further in Section 2.4. Other studies have also noted changes in CEI composition based on cut-off potential or the use of electrolyte additives

[21,35,48]. We report here for the first time that, at the same cut-off voltage (UUC = 4.5 V), dynamic cycling and static potential hold ("4.5 V cyc" and "4.5 V hold") result in markedly different CEI composition and thickness. This finding highlights that the electrochemical protocol itself is a critical- and often overlooked-factor in determining the state of the CEI. Interestingly, the minimal compositional variations and similar CEI thickness observed for the "4.5 V hold" and "4.5 V cyc+hold" samples suggest that the increase in impedance (Fig. 2) is not primarily driven by changes in the CEI, but rather to structural changes within the CAM. To validate this hypothesis, the "4.5 V cyc+hold" cathodes are analyzed via TEM and compared with previously measured "4.5 V hold" samples in

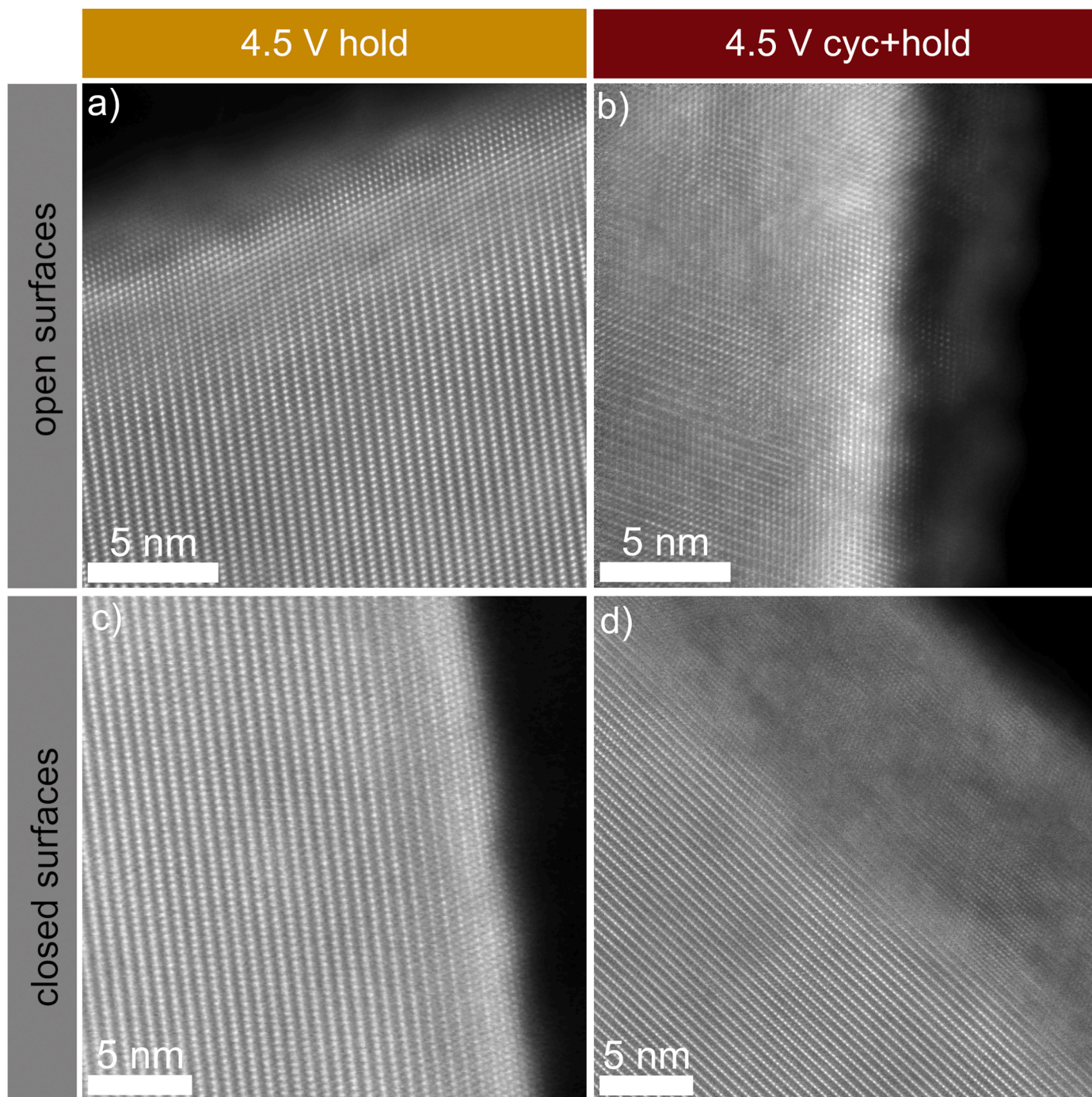


Fig. 6. HAADF STEM images of structural degradation compared between different electrochemical protocols. “Open” surfaces of a) the sample held at 4.5 V ($t_{\text{hold}} = 16$ d, 11 cycles) [42] and b) the cycled sample ($t_{\text{hold}} = 16$ d, 103 cycles) and “closed” surfaces in c) and d). Both surface orientations show stronger lattice reconstruction when cycled more, especially the closed surfaces which are typically less prone to formation of rocksalt-type phase.

the following section.

2.3. Structural degradation

In our previous work, we found for "4.5 V hold" samples that major parts of the increased kinetic hindrance in the form of R_{CT} and slow Li diffusion in degraded CAMs are caused by reconstruction of the crystal lattice. This occurs under oxygen release and results in a cubic rocksalt-type phase ($Fm\bar{3}m$ space group), as also many other groups have reported [26,49]. Here, we performed high-resolution scanning TEM (HRSTEM) in high angle annular dark field (HAADF) mode on cathodes after $t_{hold} = 16$ d and 103 cycles and compared it with samples from our previous study, where only minimal cycling but various t_{hold} were investigated [42].

For the cathode that underwent 103 cycles ("4.5 V cyc+hold"), two main observations stand out, especially when comparing the STEM images with samples with the same $t_{hold} = 16$ d but less cycles, as shown in Fig. 6. First, slightly more structural degradation is observed, when the sample is additionally cycled and cation mixing is observed deeper within the bulk. The complete reconstruction of the crystal lattice toward rocksalt-type $Li_xTM_{1-x}O_1$ (close to TM_1O_1) is observed over the first few nanometers, similar to the "4.5 V hold" sample. Previously, we have found large areas of a gradual transition region, where lithium sites are occupied by TM ions (Ni_{Li}^*) but the phase is not yet fully reconstructed to TM_1O_1 [42]. These regions serve as diffuse phase boundary regions in the epitactic and coherent phase growth and appear even wider for the "4.5 V cyc+hold" sample (Fig. 6, right side). Here, TM ions are found on lithium sites even ≈ 35 nm into the particle bulk (see SI section S7.2). The main difference from the "4.5 V hold" to the "4.5 V cyc+hold" sample is the thick layer of ≈ 5 nm of rocksalt-type phase at the "closed" surfaces after additional cycling (lithium layers parallel to the surface, e.g. (003)). The observed SRL can be compared to an estimated thickness d_{RS} of an idealized "shell" of rocksalt-type phase based on electrochemical measurements ($d_{RS} \approx 17$ nm, see SI section S2.4 for calculation and underlying assumptions). The overestimation of d_{RS} might arise from CAM loss due to partial contact loss within the cathode (e.g. due to electronically insulating SRL), which is then falsely attributed to reconstructed phase.

This leads to the second main observation: The surface covering nature of the formed rocksalt-type phase after additional cycling, even at "closed" surfaces. In contrast, we have seen preferential SRL formation at "open" surfaces (lithium layers intersecting the surface, e.g. (104)) in samples held at 4.5 V ("4.5 V hold", Fig. 6 left side). This observation is consistent with previous reports showing that SRL formation is more pronounced along lithium diffusion layers [44]. Following increasing t_{hold} , we observed gradual transitions and local inhomogeneities which still allowed pathways for lithium ions from the electrolyte toward the bulk. This transition region is now found deeper in the bulk for the "4.5 V cyc+hold" sample, and an additional "shell" of rocksalt-type phase, also on "closed" surfaces is found, as often reported in studies with electrochemical protocols featuring multiple hundreds of cycles. The only surfaces with minor signs of degradation were regions where supposedly no electrolyte could enter as shown in SI section S5.1 where an apparently closed pore between two particles is shown. Finally, an interesting finding is that the cycled cathode (Fig. 6 right side) showed no signs of cracking or layer gliding, as was observed at rare spots in the sample with long t_{hold} [42].

Our analysis is based on representative STEM images (Fig. 6, SI section S7 and provided data repository) and is thus qualitative in nature. However, based on our observations, we can hypothesize that additional cycling leads to enhanced structural degradation compared to mere exposure to high potentials. Apparently, repeated phase transitions or lattice contractions/expansions, especially when charging high-Ni layered oxides above ≈ 4.1 V are more detrimental than solely staying in this strongly delithiated state [4,33,50]. We further verify that the

inhomogeneous formation of rocksalt-type phase could indeed be due to application of long potential holds, and becomes more quickly covering when applying typical cycling protocols.

The observed SRL from STEM images in the "4.5 V cyc+hold" sample can be compared to an estimated thickness d_{RS} of an idealized "shell" of rocksalt-type phase based on electrochemical measurements ($d_{RS} \approx 17$ nm, see SI section S2.4 for calculation and underlying assumptions). From our observations and this comparison, we hypothesize several factors influencing R_{CT} as a function on the SRL properties. First, the distribution of reconstructed CAM plays an important role [5,26,44,51,52]. Based on the cited literature, surface coverage appears more detrimental than bulk reconstruction (for charge transfer). Secondly, the specific resistance/ionic conductivity of reconstructed lattice depends on its composition and structure. A small residual trace of Li atoms in the reconstructed phase ($Li_xTM_{1-x}O_1$) or a region with high amounts of defects may show a higher ionic conductivity than pure rocksalt-type phase (TM_1O_1), even though they appear very similar in STEM images. This could explain the difference of the estimated $d_{RS} = 17$ nm of assumed pure rocksalt-type phase compared to 35 nm of cation-mixing region. Another explanation for the overestimation of d_{RS} from CAM loss might arise from partial contact loss within the cathode (e.g. due to electronically insulating SRL), which is then falsely attributed to reconstructed phase.

While our observations do not allow a quantification of the impact of the SRL composition and distribution on R_{CT} directly, the drastic increase in charge transfer resistance with the covering of the LE|NCM interface with the resistive rocksalt-type phase is clearly correlated [53].

2.4. Discussion on NCM degradation mechanism under various aging protocols and relevance for other systems

In this final section, we summarize our results in a mechanistic sketch and place our observations within the context of current literature to revisit potential mechanisms for SRL and CEI formation. We also discuss the role of the CEI, as well as the potential implications of our results for other battery systems.

With the new insight from this study, we can extend the mechanistic sketch from our previous publication shown in Fig. 7 and describe how the CEI and SRL formation changes qualitatively depending on the electrochemical protocol [42].

Upon contact with the electrolyte at OCV, an initial CEI forms, consisting of LiF, organic compounds (e.g., $C_xH_yO_z$), and minor inorganic species (Al_xF_y and NiF_2), while the underlying NCM structure

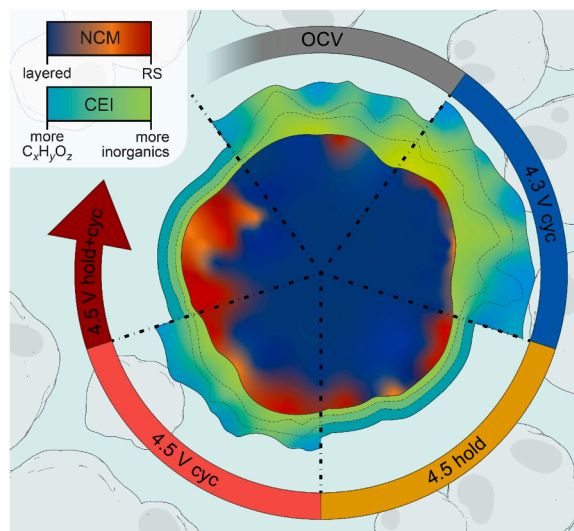


Fig. 7. Schematic of the influence of cycling conditions on the LE|NCM interface. Credit: Elisa Monte/JLU Giessen.

remains unchanged. Upon cycling to 4.3 V, the degradation of the electrolyte solvent accelerates, leading to the formation of a thick, organic-rich layer that incorporates the initial inorganic components, resulting in a more intermixed and less distinctly layered CEI. We believe that even at this potential, some structural degradation occurs, leading to the formation of an inhomogeneous SRL at the interface. As we proposed previously, this SRL begins to constrict Li-ion pathways, causing a (nonlinear, *i.e.*, initially slow) rise in charge transfer resistance. When U_{UC} is increased to 4.5 V, this constriction effect worsens. The faster degradation at higher potentials leads to a more extensive, but still inhomogeneous, SRL. A significant change also occurs in the CEI: The organic part becomes unstable and is partially removed, while the fraction of inorganic components (Al_xF_y and NiF_2) increases. This indicates that the CEI is actively being oxidized and restructured at this high potential. Holding the cathode at a constant 4.5 V potential reveals different dynamics. The capacity fade over time is less severe compared to cycling, which corresponds to slower SRL formation. However, the CEI continues to evolve. The organic components are further oxidized and dissolved, and salt degradation products (*e.g.*, $Li_xPO_yF_z$) accumulate, leaving a thin, predominantly inorganic CEI.

Finally, by combining cycling with potential holds at 4.5 V, we observe the most drastic impedance increase. This is driven by the formation of an even more extensive SRL, which is clearly caused by the dynamic stress of cycling. The CEI, however, remains similar in composition to that formed during a static hold. This suggests that the significant impedance increase is mainly a result from the growth of the SRL, while the evolution of the CEI appears to play a minor role for the overall increase in the charge transfer resistance. While our analysis primarily focuses on the evolution of charge transfer resistance, we also estimated a loss of active material during aging. This loss may stem from several mechanisms, including contact loss, transition metal dissolution, or rocksalt-type phase formation. Furthermore, as demonstrated by Xu *et al.*, the formation of a surface rocksalt-type layer can lead to 'c-axis pinning', limiting the maximum SoC of approximately 75% for certain particles within the cathode [54]. Although our current results do not allow us to definitively isolate the primary cause of this active material loss, the extensive SRL formation observed suggests that surface-induced bulk fatigue or the formation of electrochemically inactive rocksalt-type layer are likely contributors.

Our study motivates a revisit of the mechanistic understanding of SRL formation. The literature gives indications that oxygen release (formation of $V_O^{\bullet\bullet}$) and Ni migration to Li sites (formation of Ni_{Li}^{\bullet}) play important roles. Both processes are closely intertwined, *e.g.* resulting $V_O^{\bullet\bullet}$ facilitate formation of Ni_{Li}^{\bullet} and *vice versa* [27,28,30]. From our experiments, it could be understood that the crystallographic changes during cycling (*e.g.*, phase transitions) facilitate SRL formation, either via enhancing Ni_{Li}^{\bullet} formation or by enabling faster oxygen diffusion (via $V_O^{\bullet\bullet}$), which in turn increases the fraction of Ni_{Li}^{\bullet} . The exact mechanism where either oxygen or TM migration are the rate determining step of SRL formation is unclear for now. The Ni ion movement seems to be critical, as other studies on dopants suggest their stabilizing effect is purely kinetic, hindering the movement of Ni ions rather than changing the oxygen activity in the lattice [55]. From the inhomogeneity of the SRL reaction front (which moves toward the particle bulk), it appears as if a flux towards the reaction front from the particle bulk is the limiting step of SRL formation and not the outward diffusion of oxygen originating from the front [56].

While our results clarify the role of the SRL, they also raise open questions about its growth. It remains unclear if the growth mechanism itself is changing between static holds and dynamic cycling. One hypothesis is that a long potential hold leads to localized, inhomogeneous SRL growth at the most reactive sites, whereas the constant stress of cycling promotes a more homogeneous and covering layer. An alternative explanation is that the growth mechanism is the same, but the rate at which the SRL forms is simply much faster during cycling. In this

context, the repetitive 'lattice breathing' and anisotropic strain associated with crossing the remnant H2–H3 phase boundary during cycling could act as a kinetic catalyst for surface reconstruction, potentially lowering the activation energy for lattice oxygen release compared to a potential hold. Further investigation is needed to distinguish between these possibilities.

For the CEI, its thinning at high potentials could be explained by two possible mechanisms: oxidation by singlet oxygen released during SRL formation [38,41], or direct oxidation by the highly polarized Ni–O bonds in the delithiated cathode [39]. Both mechanisms can result in the oxidative decomposition of the CEI. Based on our results we hypothesize that the latter plays a more significant role: The CEI is thinnest and most inorganic after a long potential hold, where SRL formation (and thus oxygen release) is slower than in the cycled cell. This implies that the sustained high potential itself is the primary driver for oxidizing and removing the organic CEI components over time. Regarding the fate of these oxidative decomposition products of the CEI, we hypothesize, based on the provided references, that Li_2CO_3 and organic carbonates can undergo further oxidation at high voltages (>4.3 V *versus* Li^+/Li). This often results in the evolution of CO_2 and CO gases, as evidenced by OEMS studies [38,57–60]. Specifically, the reaction of the electrolyte with singlet oxygen results in the formation of CO_2 , CO , and H_2O [61]. Whether they derive from the decomposition of the solid CEI or the bulk electrolyte, remains a significant analytical challenge. Furthermore, chemical dissolution may occur; species like lithium alkyl carbonates or certain $Li_xPO_yF_z$ fragments are known to have limited solubility in carbonate based electrolytes. The literature suggests a dynamic equilibrium where CEI components continuously dissolve and reprecipitate [38,39]. Additionally, the oxidation products of alcohols (aldehydes and carboxylic acids), the hydration of aldehydes to form acetals, and the formation of fluoroethylene carbonate (FEC) from vinylencarbonat (VC) appear to be soluble in the electrolyte upon formation [61]. Based on these presented studies which focus on the degradation of the electrolyte we assume that the oxidative decomposition products of the CEI can dissolve into the electrolyte and be evolved as gaseous species.

At first glance, our results indicate that for the degradation of the NCM the electrolyte does not play an important role due to the SRL being the main degradation mechanism resulting in impedance growth. We still believe that the electrolyte and the CEI forming on the NCM play an important role for the overall stability of the NCM and electrolyte. We distinguish three degradation pathways where the CEI plays an important role. **Electrolyte attack at the NCM:** This primarily involves HF induced transition metal dissolution and surface fluorination. **NCM instability:** The chemical formation of the SRL and the release of singlet oxygen driven by the thermodynamic instability of the highly delithiated Ni-rich phase. **NCM driven electrolyte degradation:** The electrolyte oxidizes due to the reaction at the NCM, driven by oxygen release or the catalytic effect of the polarized Ni–O bond.

Crucially, an optimized electrolyte can stabilize the NCM surface by suppressing the oxygen release that accompanies SRL formation. This mitigation is achieved either through the formation of a CEI, which provides a kinetic barrier, or through favorable interfacial energetics. Specifically, lowering the energy level of the highest occupied molecular orbital (HOMO) of the electrolyte makes oxygen evolution thermodynamically less favored [5,62–64]. Furthermore, the CEI protects the interface by shielding the NCM from HF attack while simultaneously protecting the electrolyte from oxidation by the NCM. Tuning the CEI by optimizing the electrolyte formulation with additives or applying surface coatings to the NCM can, therefore, lead to enhanced overall stability, mitigating both R_{CT} increase and capacity fading. We believe that while the three primary degradation pathways still occur, the CEI serves to modulate the rates at which they proceed. Further specialized studies are required to identify how specific CEI compositions influence the kinetics of these individual degradation mechanisms.

An important consideration is how our study on half-cells, which focuses solely on cathode degradation, translates to commercial full-cell

lithium-ion batteries. We employed a high potential (4.5 V versus Li^+/Li) and an additive-free electrolyte, half-cell configuration to isolate and accelerate the intrinsic degradation mechanisms of the NCM cathode. While these conditions are more extreme than typical operating windows, they provide a fundamental understanding of the degradation occurring at the cathode. The prolonged holds at high potential serve as an accelerated aging test, and by excluding complicating factors like anode crosstalk and the influence of electrolyte additives, we can attribute the observed impedance growth to changes at the cathode itself. We believe the SRL formation represents an intrinsic degradation mechanism of the NCM material and influences the performance of high-Ni cathodes, regardless of half-cell or full-cell testing. In essence, while the quantitative rates of degradation will vary, the fundamental mechanism, the formation of a resistive surface layer in the cathode particles, applies to all cell configurations. Although modern high-nickel materials are already well stabilized and exhibit long cycle life, the understanding of the underlying degradation mechanisms lags behind these practical advancements.

3. Conclusions

Detailed electrochemical investigations and multi-method *post mortem* analyses were performed on single-crystal NCM831106 cathodes subjected to different cycling and high-voltage hold protocols. We identify that the main detrimental effects are of a kinetic nature, with impedance growth driven primarily by the number of high-voltage cycles rather than the time spent at high potential. The charge transfer resistance of the cathode increases nonlinearly with progressive cycling, which is correlated with the accelerated growth of a rocksalt-type SRL, as revealed by structural analysis via TEM. In contrast, combined XPS and SIMS analyses show that the CEI becomes thinner and more inorganic under high-voltage conditions and does not correlate with the impedance increase. Crucially, despite showing different charge transfer resistances, cathodes subjected to different ageing protocols form similar CEI compositions. This lack of correlation suggests that the CEI plays a minor role for the impedance growth. Consequently, we conclude that the nonlinear increase in charge transfer resistance is a consequence of SRL growth. The SRL constricts Li-ion pathways, creating a kinetic bottleneck that forms significantly faster under the dynamic stress of cycling. Our study tries to differentiate the effects of dynamic cycling from static calendar aging. Overall, these results contribute to a more detailed understanding of high-Ni CAM degradation, highlighting that the SRL is a primary driver of the kinetic limitations of LIBs, while the influence of the CEI remains comparatively minor under these conditions.

4. Experimental section

4.1. Cathode preparation and cell construction

As CAM we used single-crystalline $\text{LiNi}_{0.83}\text{Co}_{0.11}\text{Mn}_{0.06}\text{O}_2$ (MSE Supplies LLC, Tucson, USA) which has a specific surface area of $(0.61 \pm 0.01) \text{ m}^2/\text{g}$, as measured by Krypton Brunauer-Emmett-Teller measurement (BET) and an approximate mean particle size of $1 \mu\text{m}$, as estimated from SEM images. The pristine powder showed 0.34 wt% of LiOH on the material surface and no detectable Li_2CO_3 residuals during acid titration. Furthermore, it shows zirconium doping and a borate coating in XPS survey scans.

Cathode preparation followed the procedure described in our previous publication [42]. To probe CAM related processes rather than electrode properties, we chose low cathode loadings of $\sim 4 \text{ mg}/\text{cm}^2$, corresponding to $1.1 \text{ mAh}/\text{cm}^2$ ($275.1 \text{ mAh}/\text{g}$) or to $0.8 \text{ mAh}/\text{cm}^2$ ($200 \text{ mAh}/\text{g}$). Cycling currents were calculated based on the latter.

For simple cell testing, CR2032 coin cells were used with aluminum coating on the cathode casing to avoid reactions with steel components at high potentials. At the anode side, a stainless-steel spacer and a

lithium chip (MSE Supplies LLC, Tucson, USA) with a diameter of 14 mm and a thickness of $600 \mu\text{m}$ were used after mechanically removing the passivation layer from the lithium. For separators, we employed glass fiber pads (GF/D – Whatman, Global Life sciences solutions USA LLC, Marlborough, USA) with $70 \mu\text{L}$ of LP40 (1 M LiPF_6 in EC:DEC = 50 v:50 v, MU Ionic Solutions Corporation, Tokyo, Japan) and a Celgard® 2325 (Celgard LLC, Charlotte, North Carolina, USA) separator at the cathode side to avoid glass fibers interfering with *post mortem* analysis.

To investigate impedance evolution, 3-electrode cells in pouch bags with 20 hPa vacuum were assembled. For that an insulated gold wire with a burnt tip ($50 \mu\text{m}$ thickness, Goodfellow GmbH, Hamburg, Germany) and an additional glass fiber separator were introduced between anode and cathode as reference electrode. For lithiation, a current between the lithium anode and the Au wire was applied until the potential reached 200 mV versus Li^+/Li resulting in an equilibrium potential of $\approx 310 \text{ mV}$ versus Li^+/Li . PEIS measurements were conducted at various potentials after 200 kHz to 10 MHz with an amplitude of 10 mV using two measurements per frequency and the Biologics built-in drift correction.

4.2. Cathode sample and electrochemical protocols

Table 1 shows the cathode samples and their respective electrochemical protocol. For each cell, duplicate coin cells were assembled, and to investigate impedance evolution for the “4.5 V cyc”, “4.5 V cyc+hold” samples, at duplicate 3-electrode cells were tested and compared to our previous 3-electrode cells with various t_{hold} [42]. For more details regarding the comparison of 2- and 3-electrode cells refer to SI Table S1. For initial formation, the cells were cycled two times between 3 V and U_{UC} (either 4.3 or 4.5 V) with 0.1C and 2 h holds at U_{UC} . Then, different cycling protocols according to Table 1 were performed. Before cathode harvesting for *post mortem* analysis, all cathodes were charged to 3.7 V and held there for at least 12 h to ensure comparable SoC. The cells were opened under Ar atmosphere and one cathode for each electrochemical protocol was washed in pure DEC for ~ 1 min, rinsed carefully with fresh DEC and finally dried in vacuum for 10 min. For a detailed discussion on how sample preparation protocols (particularly washing) may influence the surface analysis, see SI Section S3.

4.3. ToF-/Orbitrap-SIMS

For the analysis, washed cathode samples were mounted on a Leica stub using double-sided adhesive tape (Tesa SE, Norderstedt, Germany). All SIMS measurements were conducted with a ToF-SIMS M6 hybrid instrument (IONTOF GmbH, Münster, Germany). To prevent atmospheric exposure, the samples were transferred into the instrument's ultra-high vacuum chamber under an Ar atmosphere utilizing a Leica EM VCT500 shuttle (Leica Mikrosysteme GmbH, Wetzlar, Germany).

Surface spectra were acquired in negative ion polarity with the liquid metal ion gun (LMIG) operating in a pulsed, spectrometry mode with a 30 kV Bi^{3+} primary ion source. This configuration generated a signal intensity of approximately 100,000 counts/s and achieved a mass resolution ($m/\Delta m$) of ≈ 5300 at $m/z = 19.00 \text{ u}$ (F^-). A low-energy electron flood gun was used for charge compensation. The analysis area was set to $150 \times 150 \mu\text{m}^2$, rastered with 64×64 pixels, and a cycle time of 85 μs was used, corresponding to a mass range of $m/z = 0\text{--}394 \text{ u}$. To operate under static SIMS conditions, the primary ion current was maintained at $I \approx 0.066 \text{ pA}$, ensuring the total ion dose remained below the 5×10^{11} ions/ cm^2 limit. The resulting spectra were mass-calibrated using known fragments, including Li^- , F^- , Cl^- , NiO_2^- , C_8^- , and PF_6^- . For the subsequent principal component analysis (PCA), a data matrix was constructed from 90 manually selected mass fragments (listed in the SI) after normalization to total ion counts.

Depth profiling was performed in Orbitrap-SIMS mode to mitigate topographical effects. In this configuration, the LMIG was operated in a long-pulse mode, using a 15 kV Bi primary beam directed through a 400

μm aperture. Secondary ions were analyzed using an attached Orbitrap Q Exactive™ mass spectrometer (Thermo Fisher Scientific Inc., Waltham, USA). The profiles were acquired over a $450 \times 450 \mu\text{m}^2$ area for a duration of 900 s, with a primary ion current of approximately $I \approx 600$ pA. This setup covered a mass range of $m/z = 50\text{--}750$ u and provided an ultra-high mass resolution of $m/\Delta m \approx 407,866$ at $m/z = 78.9587$ u (PO_3^-). The Orbitrap mass axis was calibrated using an internal silver reference. It should be noted that interpreting depth profiles in mixed organic and inorganic layers is challenging, as the sputter yield is highly dependent on the material matrix, with organic components generally being removed faster than inorganic ones.

4.4. XPS

X-ray photoelectron spectroscopy (XPS) was performed using a PHI VersaProbe IV instrument (ULVAC-PHI, Chigasaki, Japan). For the analysis, washed cathode samples were mounted onto the sample holder with double-sided adhesive tape (Tesa SE, Norderstedt, Germany). To prevent air exposure, the samples were introduced into the analysis chamber via a dedicated Ar-filled transport vessel. The instrument was equipped with a monochromatic Al- K_{α} X-ray source (1486.6 eV), which was operated at 15 kV and 50 W with a beam diameter of 200 μm . High-resolution core-level spectra were recorded for F 1 s, Li 1 s, C 1 s, O 1 s, P 2p, Al 2p, Ni 2p, Mn 2p, and Co 2p using a pass energy of 55 eV and a step size of 0.2 eV. The binding energy scale of all spectra was referenced to the adventitious carbon C 1 s peak at 285.0 eV.

4.5. TEM

TEM samples of the electrodes were prepared by dual-beam focused ion beam (FIB, Helios NanoLab 460F1, FEI, Eindhoven, Netherlands) using a 5–30 kV Ga ion beam. A carbon coating of 2 nm was applied as protection layer. After the lift-out, the lamella was thinned to 1 μm thickness by applying 30 kV. Subsequently, the voltage was reduced to 16 kV to minimize beam-damage effects. A final polishing step was performed at 5 kV. All lamellas reached a thickness of <100 nm. The lamellas were stored under vacuum and subjected to Ar plasma cleaning immediately prior to their transfer to the TEM. HAADF-STEM images were obtained with an aberration-corrected TEM (Spectra 30–300, Thermo Fisher Scientific Inc., Waltham, USA) operated at 200 kV and 300 kV, with a current of approximately 25 pA and a convergence angle of 25.4 mrad.

Declaration of generative AI and AI-assisted technologies in the writing process

During the preparation of this work, the authors used large language models to improve readability and language. After using this tool, the authors reviewed and edited the content as needed and take full responsibility for the content of the publication.

CRediT authorship contribution statement

Steffen Schröder: Writing – original draft, Visualization, Methodology, Investigation, Formal analysis, Data curation, Conceptualization. **Kilian Vettori:** Writing – original draft, Visualization, Methodology, Investigation, Formal analysis, Data curation, Conceptualization. **Lara Ahrens:** Writing – review & editing, Methodology, Investigation, Formal analysis, Data curation. **Torsten Brezesinski:** Writing – review & editing. **Aleksandr Kondrakov:** Writing – review & editing. **Joachim Mayer:** Writing – review & editing. **Jürgen Janek:** Writing – review & editing, Supervision, Funding acquisition. **Anja Hens:** Writing – review & editing, Supervision, Funding acquisition.

Declaration of competing interest

The authors declare that they have no known competing financial interests or personal relationships that could have appeared to influence the work reported in this paper.

Acknowledgements

The authors gratefully acknowledge funding by the BMFT (Federal Ministry for Research, Technology and Space, Germany) within the AQUA-POP project (grant no. 03XP0329B). Financial support (AK, JJ, TB) by BASF SE (Ludwigshafen, Germany) is also gratefully acknowledged. Open access funding enabled and organized by Projekt DEAL.

Supplementary materials

Supplementary material associated with this article can be found, in the online version, at [doi:10.1016/j.ensm.2026.105115](https://doi.org/10.1016/j.ensm.2026.105115).

Data availability

The raw data will be shared at the open access repository JLUdata at: <https://doi.org/10.22029/jlupub-20571>.

References

- [1] S.S. Zhang, Problems and their origins of Ni-rich layered oxide cathode materials, *Energy Storage Mater.* 24 (2020) 247–254, <https://doi.org/10.1016/j.ensm.2019.08.013>.
- [2] X. Han, L. Lu, Y. Zheng, X. Feng, Z. Li, J. Li, M. Ouyang, A review on the key issues of the lithium ion battery degradation among the whole life cycle, *eTransportation* 1 (2019) 100005, <https://doi.org/10.1016/j.etrans.2019.100005>.
- [3] L. de Biasi, A.O. Kondrakov, H. Gebwein, T. Brezesinski, P. Hartmann, J. Janek, Between Scylla and Charybdis: balancing among structural stability and energy density of layered NCM cathode materials for advanced lithium-ion batteries, *J. Phys. Chem. C* 121 (2017) 26163–26171, <https://doi.org/10.1021/acs.jpcc.7b06363>.
- [4] H.-J. Noh, S. Youn, C.S. Yoon, Y.-K. Sun, Comparison of the structural and electrochemical properties of layered Li[Ni_xCoyMnz]O₂ ($x = 1/3, 0.5, 0.6, 0.7, 0.8$ and 0.85) cathode material for lithium-ion batteries, *J. Power Sources* 233 (2013) 121–130, <https://doi.org/10.1016/j.jpowsour.2013.01.063>.
- [5] D.-S. Ko, J.-H. Park, B.Y. Yu, D. Ahn, K. Kim, H.N. Han, W.S. Jeon, C. Jung, A. Manthiram, Degradation of high-nickel-layered oxide cathodes from surface to bulk: a comprehensive structural, chemical, and electrical analysis, *Adv. Energy Mater.* 10 (2020) 2001035, <https://doi.org/10.1002/aenm.202001035>.
- [6] S. Barcellona, S. Colnago, G. Dotelli, S. Latorrata, L. Piegari, Aging effect on the variation of Li-ion battery resistance as function of temperature and state of charge, *J. Energy Storage* 50 (2022) 104658, <https://doi.org/10.1016/j.jest.2022.104658>.
- [7] J. Zhu, M.S. Dewi Darma, M. Knapp, D.R. Sørensen, M. Heere, Q. Fang, X. Wang, H. Dai, L. Mereacre, A. Senyshyn, X. Wei, H. Ehrenberg, Investigation of lithium-ion battery degradation mechanisms by combining differential voltage analysis and alternating current impedance, *J. Power Sources* 448 (2020) 227575, <https://doi.org/10.1016/j.jpowsour.2019.227575>.
- [8] A. Barré, B. Deguilhem, S. Grolleau, M. Gérard, F. Suard, D. Riu, A review on lithium-ion battery ageing mechanisms and estimations for automotive applications, *J. Power Sources* 241 (2013) 680–689, <https://doi.org/10.1016/j.jpowsour.2013.05.040>.
- [9] M.S.D. Darma, M. Lang, K. Kleiner, L. Mereacre, V. Liebau, F. Fauth, T. Bergfeldt, H. Ehrenberg, The influence of cycling temperature and cycling rate on the phase specific degradation of a positive electrode in lithium ion batteries: a post mortem analysis, *J. Power. Sources* 327 (2016) 714–725, <https://doi.org/10.1016/j.jpowsour.2016.07.115>.
- [10] J. Kasnatscheew, M. Evertz, B. Streipert, R. Wagner, S. Nowak, I. Cekic Laskovic, M. Winter, Improving cycle life of layered lithium transition metal oxide (LiMO₂) based positive electrodes for Li ion batteries by smart selection of the electrochemical charge conditions, *J. Power. Sources* 359 (2017) 458–467, <https://doi.org/10.1016/j.jpowsour.2017.05.092>.
- [11] Y. Yang, R. Xu, K. Zhang, S.-J. Lee, L. Mu, P. Liu, C.K. Waters, S. Spence, Z. Xu, C. Wei, D.J. Kautz, Q. Yuan, Y. Dong, Y.-S. Yu, X. Xiao, H.-K. Lee, P. Pianetta, P. Cloetens, J.-S. Lee, K. Zhao, F. Lin, Y. Liu, Quantification of heterogeneous degradation in Li-ion batteries, *Adv. Energy Mater.* 9 (2019) 1900674, <https://doi.org/10.1002/aenm.201900674>.
- [12] A. Mikheenkova, A.J. Smith, K.B. Frenander, Y. Tesfamhret, N.R. Chowdhury, C.-W. Tai, T. Thiringer, R.W. Lindström, M. Hahlin, M.J. Lacey, Ageing of high energy density automotive Li-ion batteries: the effect of temperature and State-of-charge, *J. Electrochem. Soc.* 170 (2023) 80503, <https://doi.org/10.1149/1945-7111/aceb8f>.

- [13] J. Dutta, S. Ghosh, S.K. Martha, A short review on fast charging of Ni-rich layered oxide cathodes, *J. Solid. State Electrochem.* (2024), <https://doi.org/10.1007/s10008-024-06031-0>.
- [14] Y. Song, L. Wang, L. Sheng, D. Ren, H. Liang, Y. Li, A. Wang, H. Zhang, H. Xu, X. He, The significance of mitigating crosstalk in lithium-ion batteries: a review, *Energy Environ. Sci.* 16 (2023) 1943–1963, <https://doi.org/10.1039/d3ee00441d>.
- [15] A. Manthiram, A reflection on lithium-ion battery cathode chemistry, *Nat. Commun.* 11 (2020) 1550, <https://doi.org/10.1038/s41467-020-15355-0>.
- [16] M.D. Radin, S. Hy, M. Sina, C. Fang, H. Liu, J. Vinckeviciute, M. Zhang, M. S. Whittingham, Y.S. Meng, A. van der Ven, Narrowing the gap between theoretical and practical capacities in Li-ion layered oxide cathode materials, *Adv. Energy Mater.* 7 (2017) 1602888, <https://doi.org/10.1002/aenm.201602888>.
- [17] M.J.W. Ogley, B.L.J. Johnston, D.S. Hall, L.F.J. Piper, Understanding degradation in single-crystalline Ni-rich Li-ion battery cathodes, *Chem. Rev.* 125 (2025) 9774–9806, <https://doi.org/10.1021/acs.chemrev.5c00330>.
- [18] S. Ma, X. Zhang, S. Wu, E. Fan, J. Lin, R. Chen, F. Wu, L. Li, Unraveling the nonlinear capacity fading mechanisms of Ni-rich layered oxide cathode, *Energy Storage Mater.* 55 (2023) 556–565, <https://doi.org/10.1016/j.ensm.2022.12.009>.
- [19] J. Vetter, P. Novák, M.R. Wagner, C. Veit, K.-C. Möller, J.O. Besenhard, M. Winter, M. Wohlfahrt-Mehrens, C. Vogler, A. Hammouche, Ageing mechanisms in lithium-ion batteries, *J. Power Sources* 147 (2005) 269–281, <https://doi.org/10.1016/j.jpowsour.2005.01.006>.
- [20] S. Lee, W. Li, A. Dolocan, H. Celio, H. Park, J.H. Warner, A. Manthiram, In-depth analysis of the degradation mechanisms of high-nickel, low/No-cobalt layered oxide cathodes for lithium-ion batteries, *Adv. Energy Mater.* 11 (2021) 2100858, <https://doi.org/10.1002/aenm.202100858>.
- [21] S. Jeon, G. Lim, H. Lee, H. Park, M.K. Cho, C. Kim, Y. Lee, J. Kim, M. Kwon, J.-K. Yoo, H. Jeong, J. Kim, S.-H. Yu, M. Lee, J. Kim, J. Hong, Reduction-induced oxygen loss: the hidden surface reconstruction mechanism of layered oxide cathodes in lithium-ion batteries, *Adv. Energy Mater.* 15 (2025) 2404193, <https://doi.org/10.1002/aenm.202404193>.
- [22] S. Wu, X. Zhang, S. Ma, E. Fan, J. Lin, R. Chen, F. Wu, L. Li, A new insight into the capacity decay mechanism of Ni-rich layered oxide cathode for lithium-ion batteries, *Small* 18 (2022) e2204613, <https://doi.org/10.1002/sml.202204613>.
- [23] H. Zhang, H. Liu, L.F.J. Piper, M.S. Whittingham, G. Zhou, Oxygen loss in layered oxide cathodes for Li-ion batteries: mechanisms, effects, and mitigation, *Chem. Rev.* 122 (2022) 5641–5681, <https://doi.org/10.1021/acs.chemrev.1c00327>.
- [24] K. Ishizu, Y. Oka, T. Nakamura, Lattice volume change during charge/discharge reaction and cycle performance of Li[NixCoyMnz]O₂, *Solid State Ion* 288 (2016) 176–179, <https://doi.org/10.1016/j.ssi.2016.01.009>.
- [25] H.-H. Ryu, K.-J. Park, C.S. Yoon, Y.-K. Sun, Capacity fading of Ni-rich Li[Ni_xCo_yMn_{1-x-y}]O₂ (0.6 ≤ x ≤ 0.95) cathodes for high-energy-density lithium-ion batteries: bulk or surface degradation? *Chem. Mater.* 30 (2018) 1155–1163, <https://doi.org/10.1021/acs.chemmater.7b05269>.
- [26] S. Schweidler, L. de Biasi, G. Garcia, A. Mazilkin, P. Hartmann, T. Brezesinski, J. Janek, Investigation into mechanical degradation and fatigue of high-Ni NCM cathode material: a long-term cycling study of full cells, *ACS Appl. Energy Mater.* 2 (2019) 7375–7384, <https://doi.org/10.1021/acsami.9b01354>.
- [27] X. Hou, K. Ohta, Y. Kimura, Y. Tamenori, K. Tsuruta, K. Amezawa, T. Nakamura, Lattice oxygen instability in oxide-based intercalation cathodes: a case study of layered LiNi_{1/3}Co_{1/3}Mn_{1/3}O₂, *Adv. Energy Mater.* 11 (2021) 2101005, <https://doi.org/10.1002/aenm.202101005>.
- [28] X.-Y. Hou, Y. Kimura, Y. Tamenori, K. Nitta, H. Yamagishi, K. Amezawa, T. Nakamura, Thermodynamic analysis enables quantitative evaluation of lattice oxygen stability in Li-ion battery cathodes, *ACS Energy Lett.* 7 (2022) 1687–1693, <https://doi.org/10.1021/acsenergylett.2c00353>.
- [29] N.A. Shah, G.J. Páez Fajardo, H. Banerjee, G.C. Pandey, A.S. Menon, M. Ans, V. Majherova, G. Bree, S. Bolloju, D.C. Grinter, P. Ferrer, P.K. Thakur, T.-L. Lee, M. J. Lovridge, A.J. Morris, C.P. Grey, L.F.J. Piper, Nature of the oxygen-loss-induced rock salt layer and its impact on capacity fade in Ni-rich layered oxide cathodes, *ACS Energy Lett.* 10 (2025) 1313–1320, <https://doi.org/10.1021/acsenergylett.5c00324>.
- [30] I. Takahashi, T. Maeda, H. Kiuchi, K. Nakanishi, A. Ohma, M. Hatano, T. Fukunaga, T. Ohta, E. Matsubara, Mechanism of structural change and the trigger of electrochemical degradation of Li-rich layered oxide cathodes during charge-discharge cycles, *ACS Appl. Energy Mater.* 2 (2019) 8118–8124, <https://doi.org/10.1021/acsami.9b01595>.
- [31] A. Schürmann, B. Luerßen, D. Mollenhauer, J. Janek, D. Schröder, Singlet Oxygen in electrochemical cells: a critical review of literature and theory, *Chem. Rev.* 121 (2021) 12445–12464, <https://doi.org/10.1021/acs.chemrev.1c00139>.
- [32] J. Wandt, A.T. Freiberg, A. Ogrodnik, H.A. Gasteiger, Singlet oxygen evolution from layered transition metal oxide cathode materials and its implications for lithium-ion batteries, *Mater. Today* 21 (2018) 825–833, <https://doi.org/10.1016/j.mattod.2018.03.037>.
- [33] R. Jung, M. Metzger, F. Maglia, C. Stinner, H.A. Gasteiger, Oxygen release and its effect on the cycling stability of LiNi_xMn_yCo_zO₂ (NMC) cathode materials for Li-ion batteries, *J. Electrochem. Soc.* 164 (2017) A1361–A1377, <https://doi.org/10.1149/2.0021707jes>.
- [34] X. Liu, Y. Qian, X. Qi, Q. Lan, J. Jiang, Operation condition dependent degradation effects of Li-rich layered oxide/graphite-SiO_x pouch-type batteries: an in-situ and ex-situ analyses, *Electrochim. Acta* 520 (2025) 145866, <https://doi.org/10.1016/j.electacta.2025.145866>.
- [35] Y. Preger, H.M. Barkholtz, A. Fresquez, D.L. Campbell, B.W. Juba, J. Román-Kustas, S.R. Ferreira, B. Chalamala, Degradation of commercial lithium-ion cells as a function of chemistry and cycling conditions, *J. Electrochem. Soc.* 167 (2020) 120532, <https://doi.org/10.1149/1945-7111/abae37>.
- [36] Z.W. Lebens-Higgins, S. Sallis, N.V. Faenza, F. Badway, N. Pereira, D.M. Halat, M. Wahila, C. Schlueter, T.-L. Lee, W. Yang, C.P. Grey, G.G. Amatucci, L.F.J. Piper, Evolution of the electrode–Electrolyte interface of LiNi_{0.8}Co_{0.15}Al_{0.05}O₂ electrodes due to electrochemical and thermal stress, *Chem. Mater.* 30 (2018) 958–969, <https://doi.org/10.1021/acs.chemmater.7b04782>.
- [37] R. Scipioni, D. Isheim, S.A. Barnett, Revealing the complex layered-mosaic structure of the cathode electrolyte interphase in Li-ion batteries, *Appl. Mater. Today* 20 (2020) 100748, <https://doi.org/10.1016/j.apmt.2020.100748>.
- [38] W.M. Dose, I. Temprano, J.P. Allen, E. Björklund, C.A. O’Keefe, W. Li, B.L. Mehdi, R.S. Weatherup, M.F.L. de Volder, C.P. Grey, Electrolyte reactivity at the charged Ni-rich cathode interface and degradation in Li-ion batteries, *ACS Appl. Mater. Interfaces* 14 (2022) 13206–13222, <https://doi.org/10.1021/acsaami.1c22812>.
- [39] Y. Yu, P. Karayaylali, Y. Katayama, L. Giordano, M. Gauthier, F. Maglia, R. Jung, I. Lund, Y. Shao-Horn, Coupled LiPF₆ decomposition and carbonate dehydrogenation enhanced by highly covalent metal oxides in high-energy Li-ion batteries, *J. Phys. Chem. C* 122 (2018) 27368–27382, <https://doi.org/10.1021/acs.jpcc.8b07848>.
- [40] L. Hartmann, L. Reuter, L. Wallisch, A. Beiersdorfer, A. Adam, D. Goldbach, T. Teufel, P. Lamp, H.A. Gasteiger, J. Wandt, Depletion of electrolyte salt upon calendar aging of lithium-ion batteries and its effect on cell performance, *J. Electrochem. Soc.* 171 (2024) 60506, <https://doi.org/10.1149/1945-7111/ad4821>.
- [41] H. Luo, B. Zhang, H. Zhang, Q. Zheng, X. Wu, Y. Yan, Z. Li, Y. Tang, W. Hao, G. Liu, Y.-H. Hong, J. Ye, Y. Qiao, S.-G. Sun, Full-dimensional analysis of electrolyte decomposition on cathode-electrolyte interface: establishing characterization paradigm on LiNi_{0.6}Co_{0.2}Mn_{0.2}O₂ cathode with potential dependence, *J. Phys. Chem. Lett.* 14 (2023) 4565–4574, <https://doi.org/10.1021/acs.jpcclett.3c00674>.
- [42] K. Vettori, S. Schröder, L. Ahrens, R. Wilhelm, S. Kremer, J.K. Eckhardt, T. Brezesinski, A. Kondrakov, J. Mayer, A. Henss, J. Janek, Chemical and structural degradation of single crystalline high-nickel cathode materials during high-voltage holds, *Adv. Energy Mater.* 15 (2025) 2502148, <https://doi.org/10.1002/aenm.202502148>.
- [43] S. Oswald, H.A. Gasteiger, The structural stability limit of layered lithium transition metal oxides due to oxygen release at high State of charge and its dependence on the nickel content, *J. Electrochem. Soc.* 170 (2023) 30506, <https://doi.org/10.1149/1945-7111/acf8f0>.
- [44] F. Lin, I.M. Markus, D. Nordlund, T.-C. Weng, M.D. Asta, H.L. Xin, M.M. Doeff, Surface reconstruction and chemical evolution of stoichiometric layered cathode materials for lithium-ion batteries, *Nat. Commun.* 5 (2014) 3529, <https://doi.org/10.1038/ncomms4529>.
- [45] W. Li, A. Dolocan, P. Oh, H. Celio, S. Park, J. Cho, A. Manthiram, Dynamic behaviour of interphases and its implication on high-energy-density cathode materials in lithium-ion batteries, *Nat. Commun.* 8 (2017) 14589, <https://doi.org/10.1038/ncomms14589>.
- [46] J. Langdon, Z. Cui, A. Manthiram, Role of electrolyte in overcoming the challenges of LiNiO₂ cathode in lithium batteries, *ACS Energy Lett.* 6 (2021) 3809–3816, <https://doi.org/10.1021/acsenergylett.1c01714>.
- [47] C. Liu, A. Dolocan, Z. Cui, A. Manthiram, Multi-scale analysis of interphase chemistry for enhanced fast-charging of lithium-ion batteries with ion mass spectrometry, *J. Am. Chem. Soc.* 147 (2025) 6023–6036, <https://doi.org/10.1021/jacs.4c16561>.
- [48] J. Li, W. Li, Y. You, A. Manthiram, Extending the service life of high-Ni layered oxides by tuning the electrode–Electrolyte interphase, *Adv. Energy Mater.* 8 (2018) 1801957, <https://doi.org/10.1002/aenm.201801957>.
- [49] D. Abraham, R. Twisten, M. Balasubramanian, I. Petrov, J. McBreen, K. Amine, Surface changes on LiNi_{0.8}Co_{0.2}O₂ particles during testing of high-power lithium-ion cells, *Electrochem. Commun.* 4 (2002) 620–625, [https://doi.org/10.1016/S1388-2481\(02\)00388-0](https://doi.org/10.1016/S1388-2481(02)00388-0).
- [50] W. Li, J. Reimers, J. Dahn, *In situ* x-ray diffraction and electrochemical studies of Li_{1-x}NiO₂, *Solid State Ion* 67 (1993) 123–130, [https://doi.org/10.1016/0167-2738\(93\)90317-V](https://doi.org/10.1016/0167-2738(93)90317-V).
- [51] S.-K. Jung, H. Gwon, J. Hong, K.-Y. Park, D.-H. Seo, H. Kim, J. Hyun, W. Yang, K. Kang, Understanding the degradation mechanisms of LiNi_{0.5}Co_{0.2}Mn_{0.3}O₂ cathode material in lithium ion batteries, *Adv. Energy Mater.* 4 (2014) 1300787, <https://doi.org/10.1002/aenm.201300787>.
- [52] Z. Lun, A.J. Merryweather, A. Mahadevegowda, S.S. Pandurangi, C. Xu, S. Fairclough, V.S. Deshpande, N.A. Fleck, C. Ducati, C. Schnedermann, A. Rao, C. P. Grey, Operando single-particle imaging reveals that asymmetric ion flux contributes to capacity degradation in aged Ni-rich layered cathodes, *Energy Environ. Sci.* (2025), <https://doi.org/10.1039/d5ee00267b>.
- [53] W. Zhao, K. Wang, X. Fan, F. Ren, X. Xu, Y. Liu, S. Xiong, X. Liu, Z. Zhang, M. Si, R. Zhang, W. van den Bergh, P. Yan, C. Battaglia, T. Brezesinski, Y. Yang, Quantifying degradation parameters of single-crystalline Ni-rich cathodes in lithium-ion batteries, *Angew. Chem. Int. Engl.* 62 (2023) e202305281, <https://doi.org/10.1002/anie.202305281>.
- [54] C. Xu, K. Märker, J. Lee, A. Mahadevegowda, P.J. Reeves, S.J. Day, M.F. Groh, S. P. Emge, C. Ducati, B. Layla Mehdi, C.C. Tang, C.P. Grey, Bulk fatigue induced by surface reconstruction in layered Ni-rich cathodes for Li-ion batteries, *Nat. Mater.* 20 (2021) 84–92, <https://doi.org/10.1038/s41563-020-0767-8>.
- [55] X. Hou, T. Katsumata, Y. Kimura, Y. Tamenori, K. Nitta, H. Yamagishi, K. Amezawa, T. Nakamura, Revisiting cationic doping impacts in Ni-rich cathodes, *ACS Appl. Energy Mater.* 6 (2023) 2072–2080, <https://doi.org/10.1021/acsaem.2c04141>.
- [56] H. Schmalzried, J. Janek, Chemical kinetics of phase boundaries in solids, *Ber. Bunsenges. Phys. Chem.* 102 (1998) 127–143, <https://doi.org/10.1002/bbpc.19981020202>.

- [57] T. Hatsukade, A. Schiele, P. Hartmann, T. Brezesinski, J. Janek, Origin of carbon dioxide evolved during cycling of nickel-rich layered NCM cathodes, *ACS Appl. Mater. Interfaces* 10 (2018) 38892–38899, <https://doi.org/10.1021/acsami.8b13158>.
- [58] D. Cao, C. Tan, Y. Chen, Oxidative decomposition mechanisms of lithium carbonate on carbon substrates in lithium battery chemistries, *Nat. Commun.* 13 (2022) 4908, <https://doi.org/10.1038/s41467-022-32557-w>.
- [59] A.T.S. Freiberg, M.K. Roos, J. Wandt, R. de Vivie-Riedle, H.A. Gasteiger, Singlet oxygen reactivity with carbonate solvents used for Li-ion battery electrolytes, *J. Phys. Chem. A* 122 (2018) 8828–8839, <https://doi.org/10.1021/acs.jpca.8b08079>.
- [60] R. Wang, B. Weng, A. Mahadevegowda, I. Temprano, H. Wang, Z. He, C. Ducati, Y. Xiao, C.P. Grey, M.F.L. de Volder, Influence of carbonate electrolyte solvents on voltage and capacity degradation in Li-rich cathodes for Li-ion batteries, *Adv. Energy Mater.* 14 (2024) 2401097, <https://doi.org/10.1002/aenm.202401097>.
- [61] B.L.D. Rinkel, J.P. Vivek, N. Garcia-Araez, C.P. Grey, Two electrolyte decomposition pathways at nickel-rich cathode surfaces in lithium-ion batteries, *Energy Environ. Sci.* 15 (2022) 3416–3438, <https://doi.org/10.1039/d1ee04053g>.
- [62] L. Su, K. Jarvis, H. Charalambous, A. Dolocan, A. Manthiram, Stabilizing high-nickel cathodes with high-voltage electrolytes, *Adv. Funct. Mater.* 33 (2023) 2213675, <https://doi.org/10.1002/adfm.202213675>.
- [63] R. Pan, E. Jo, Z. Cui, A. Manthiram, Degradation pathways of cobalt-free LiNiO₂ cathode in lithium batteries, *Adv. Funct. Mater.* 33 (2023) 2211461, <https://doi.org/10.1002/adfm.202211461>.
- [64] L. Zou, Z. Liu, W. Zhao, H. Jia, J. Zheng, Y. Yang, G. Wang, J.-G. Zhang, C. Wang, Solid-Liquid interfacial reaction triggered propagation of phase transition from surface into bulk lattice of Ni-rich layered cathode, *Chem. Mater.* 30 (2018) 7016–7026, <https://doi.org/10.1021/acs.chemmater.8b01958>.